PERGAMON

Computers & Geosciences 29 (2003) 823–836

COMPUTERS & GEOSCIENCES

www.elsevier.com/locate/cageo

Image optimization and analysis of synchrotron X-ray computed microtomography (CμT) data

Dawn A. Ashbridge[a,*], Michael S. Thorne[a], Mark L. Rivers[b], Julia C. Muccino[c], Peggy A. O'Day[a]

[a] Department of Geological Sciences, Arizona State University, Tempe, AZ 85287-1404, USA
[b] Department of Geophysical Sciences and Center for Advanced Radiation Sources, University of Chicago, Chicago, IL 60637, USA
[c] Department of Civil and Environmental Engineering, Arizona State University, Tempe, AZ 85287, USA

Received 20 June 2002; accepted 10 April 2003

Abstract

Synchrotron X-ray computed microtomography (CμT) is a non-destructive technique for imaging porous and compositionally heterogeneous samples in three dimensions at the microscale. In this study, we report a package of FORTRAN algorithms for digital image optimization and three-dimensional analysis of porosity, pore connectivity, and pore structure within a CμT volume. The algorithm Tomo_optimize optimizes digital data by utilizing a series of matrix filters and contrast transforms. Tomo_classify labels individual voxels within the data set as solid, internal pore space, or external void space, thus defining virtual volume boundaries. Tomo_analysis calculates total porosity, porosity from interior pores (completely surrounded by solid), and porosity from connected pores (open to external void space), and provides an output of each pore and its pore size (number of voxels per pore). The algorithms were tested on two natural samples from hydrothermal vent chimneys. Physical volume was 116 and 72 mm^3 for each sample and CμT spatial resolution was estimated to be 57 μm. Porosity determined by the CμT algorithms was 14.1% and 15.4%, respectively. The majority of porosity (>98%) was due to connected pores rather than isolated pores, and most of the pore volume contributing to total porosity of both samples (>90%) was from one large interconnected pore. While total porosity was similar for both samples, three-dimensional visual reconstructions showed a more channelized pore structure in one sample. Sensitivity analyses were performed to test the effect of different cut-off values for air, internal pore space, and solid entered by the user before and after image processing on porosity calculations. These algorithms provide an integrated image processing and analysis package for synchrotron CμT data that should be useful for the analysis of microporous structures as this technique gains popularity.

Keywords: Image analysis; Porosity; Pore connectivity; Seafloor hydrothermal vent chimney; Three-dimensional visualization

1. Introduction

Synchrotron X-ray computed microtomography (CμT) imaging and data processing are powerful new methods for the analysis of three-dimensional digital data sets of physical volumes. Synchrotron CμT is similar to laboratory or industrial computed tomography in which a sample is imaged by passing X-rays through it over a 180° rotation, collecting the transmitted intensity (which is a function of material composition and density), and mathematically reconstructing the three-dimensional sample volume. Use of synchrotron X-rays has several advantages compared to laboratory or industrial X-ray sources. These include: (i) a high photon flux permits measurements at high spatial resolution; (ii) the X-ray source is tunable, thus

*Corresponding author. Tel.: +1-480-965-7746; fax: +1-480-965-8102.
E-mail address: ashbridge@asu.edu (D.A. Ashbridge).

0098-3004/03/$ - see front matter
doi:10.1016/S0098-3004(03)00081-5

allowing measurements at different energies; (iii) the X-ray radiation is monochromatic, which eliminates beam-hardening effects; and (iv) the beam is flat (line scanning), which simplifies the reconstruction. Methods and applications of synchrotron and conventional computerized X-ray tomography are reviewed in Wellington and Vinegar (1987), Bonse and Busch (1999), Rivers et al. (1999), and Ketcham and Carlson (2001).

A number of studies have examined natural and synthetic samples using synchrotron X-ray CμT with materials science, geological, and chemical applications. For example, bulk properties of sandstones, such as porosity, chord-length distribution, pore-size distribution, and coarseness, were determined by extracting correlation functions from the images and applying them to statistical analyses of the sample (Coker et al., 1996). Other studies have used synchrotron CμT to image void space and solid in different sandstones, vesiculated basalt, and Danish chalk on scales of 5–20 μm voxel resolution (Spanne et al., 1994; Lindquist et al., 1996, 2000; Lindquist and Venkatarangan, 1999). Algorithms calculating pore space and degree of pore connectivity have been developed for the analysis of physical properties related to fluid flow dynamics (e.g., Coker et al., 1996; Lindquist et al., 1996; Proussevitch and Sahagian, 2001). One of the first algorithms was the medial axis technique developed by Lindquist et al. (1996), in which an axis or backbone is created through the central portions of channels to form vectors representing flow paths. Other algorithms fit spheres to pore spaces or use peel-off techniques to determine object morphology (Delerue et al., 1999; Proussevitch and Sahagian, 2001).

Previous CμT studies of geologic materials have typically analyzed a binary system of void space and solid with mostly silica and silicate minerals of similar density (e.g., sandstone). Volumes with heterogeneous mixtures of minerals of different density, such as mixtures of sulfides and sulfates or carbonates, have different absorption coefficients and thus non-uniform X-ray attenuation. In addition, synchrotron radiation allows volume collection at different energies and volume subtraction to enhance contrast. This variability in materials and collection methods leads to a wide range of grayscale values within and among data sets. Image and contrast optimization can help to correctly differentiate solids of different density from each other and from void space. In tomography studies at low resolution, difficulty arises in the classification of voxels that are not completely homogeneous but fall on boundaries between solid and air, or between solids of different density (partial volume effect). Some studies, particularly in the medical field, have used mixture models to allow for sub-voxel resolution by assigning a continuum of classification values (e.g., Choi et al., 1991; Santago and Gage, 1993; Soltanian-Zadeh et al., 1993; Roll et al., 1994; Ballester et al., 2002). While mixture models are one approach, in this study we use an alternate method of image optimization and filtering to enhance contrast between solid material and void space in order to improve boundary definition, and then assign a binary classification of solid or void space based on a cut-off value chosen by the user. Owing to the high resolution achievable with synchrotron CμT but the variability in grayscale, this binary approach simplifies voxel classification by eliminating errors associated with partial voxel classification without the introduction of large errors associated with defining solid edges.

In this paper, we report algorithms for image optimization, voxel classification, and three-dimensional analysis of porosity, pore connectivity, and pore structure of a CμT volume. The algorithms are written in Fortran 90, are easy to run and modify, and allow for user input of cut-off values and processing options. While subroutines in three-dimensional image analysis programs such as Interactive Data Language® (Research Systems, Inc.) and Matlab® (Mathworks, Inc.) can be written to filter and optimize images, and to calculate and visualize porosity and pore connectivity, to our knowledge there is not a package of algorithms that accomplishes all of these steps. Numerical filters and transforms that reduce variability between slices within the three-dimensional volume (Pratt, 1978; Green, 1983) are applied before voxel classification and porosity analysis. These program features enable rapid three-dimensional analysis of heterogeneous geologic and environmental samples using synchrotron CμT at different spatial resolutions and incident energies.

2. Methods

2.1. *CμT data collection*

Two porous seafloor hydrothermal vent chimney samples (A and B) from the endeavour segment, Juan de Fuca Ridge were used for analysis (Table 1). Collection of the samples occurred in the 1998 Sulfide Recovery Program by the University of Washington, Seattle (Delaney et al., 2001). The samples came from two different hydrothermal vent chimneys with different mineral compositions and physical structures. The volume analyzed by CμT algorithms was $414 \times 414 \times 147$ voxels (of which $116\,mm^3$ was solid sample) for sample A and $568 \times 568 \times 155$ voxels (of which $72\,mm^3$ was solid sample) for sample B, which was a sub-volume of the total CμT sample volume collected (Table 1). Bulk chemical and X-ray diffraction analyses showed that sample A was a mixture of amorphous silica (SiO_2), pyrite (FeS_2), Zn sulfide (ZnS), and barite ($BaSO_4$). Sample B was a mixture of

Table 1
Sample descriptions, porosity, and pore connectivity results from CμT[a] analysis

Sample	A	B
Physical description	Visibly porous with few large channels	Visibly porous with several larger channels
Mineral description	25% amorphous silica (SiO_2), 28% pyrite (FeS_2), 46% Zn sulfide (ZnS), 1% barite ($BaSO_4$)	11% pyrite (FeS_2), 52% Zn sulfide (ZnS), 37% amorphous silica (SiO_2)
CμT sample size (mm)	$5.5 \times 7.0 \times 3.5$	$6.0 \times 15.0 \times 4.0$
Total CμT sample volume (mm^3)	135	360
CμT analysis sample volume (mm^3)	116	72
CμT porosity[b]	$14.1 \pm 3.2\%$	$15.4 \pm 2.8\%$
CμT interior pore porosity	$0.3 \pm 0.0\%$	$0.2 \pm 0.0\%$
CμT connected pore porosity	$13.8 \pm 3.2\%$	$15.2 \pm 2.6\%$

[a] CμT porosity calculated using Tomo_analysis algorithm.
[b] CμT porosity includes porosity contributions from pore volumes greater than and equal to 30,233 μm^3.

pyrite, Zn sulfide, and amorphous silica (Ashbridge, 2002). Both samples were visibly porous.

Microtomography data were collected on GeoSoilEnviroCARS (GSECARS) Sector 13 bending magnet beamline at the Advanced Photon Source (Argonne National Laboratory, IL) with a Si (2 2 0) channel cut monochromator tuned to 40 keV incident energy. A fluorescent screen downstream of the sample generated visible light that was imaged with a zoom lens onto a 12-bit charge-coupled device (CCD) camera. The readout was binned by a factor of two in each direction. Pixel size was 21.6 μm after binning.

After CμT data reconstruction, voxel size was $21.6\,\mu m \times 21.6\,\mu m \times 21.6\,\mu m$. Image resolution was estimated to be 57 μm and was determined by measuring the two nearest distinguishable objects in a two-dimensional CμT image. Voxel size determines the ability to resolve the boundary between pore and solid. Sample size is directly related to voxel size because the detector has a fixed number of pixels such that the sample will be split into a fixed number of voxels after reconstruction. Voxel volume was 10,078 μm^3 in this study. Each voxel was assigned a single attenuation value. Attenuation value is the measured linear attenuation coefficient times 10,000, for scaling, and has units of 1/voxel size (for this study 1/μm) that represent the attenuation per voxel. Attenuation coefficients are material specific and relate to the reduction in X-ray intensity after it passes through the material (Marshall, 1982). The attenuation value for each voxel represents the average of all attenuation values for each material (air and minerals) within that voxel.

2.2. Digital preprocessing

Preprocessing of CμT data is required in order to convert the CCD raw data to a three-dimensional reconstructed volume (Ackerman and Ellingson, 1991; Kinney et al., 1991; Baruchel et al., 2001). This was done using IDL software with subroutines written by GSECARS (Rivers et al., 1999).[1] The first step corrects for the CμT dark current (measured in the absence of X-rays) and white field (an image taken with X-rays in the absence of a sample). Non-uniformities in the white field due to non-uniformities in the X-ray beam, the scintillator detector response, and the CCD detector response are removed by normalizing each image to the white field image. A low-pass filter is used to remove ring artifacts (drifts or non-linear responses from detectors) from the sinograms. Conversion of the normalized CCD files into a three-dimensional volume creates a data set in the form of $[x, y, \theta]$, where θ is a range from 1° to 180° (view angle). Tomographic reconstruction was done using a Fast Fourier Transform algorithm, that converts the data to an $[x, y, z]$ array of linear attenuation coefficients.

3. Algorithms for image optimization and porosity analysis

The algorithms Tomo_optimize, Tomo_classify, and Tomo_analysis were written to allow user flexibility in optimizing image contrast, classifying pore space and solid, and calculating porosity and pore connectivity in CμT volumes. All of the programs were written in Fortran 90. The algorithms were programmed to double precision and executed on a SUN Ultra 10 workstation with an UltraSPARC-II™ processor. Each algorithm prompts the user for required inputs.

[1] GSECARS Tomography Processing Software. http://cars9.uchicago.edu/software/tomography.html

3.1. Image optimization

The range of grayscale associated with synchrotron X-ray tomography data is variable because it can be collected at different energies and it contains artifacts from non-uniformities in the X-ray beam, scintillator detector, and CCD detector. Because of this variability, the first program enables digital image processing of CμT data in order to maximize contrast between neighboring voxels in the image and to increase the range of attenuation values of the entire volume (Pratt, 1978; Green, 1983). For the two volume data sets analyzed here, the lowest attenuation value was different because voxels outside the tomographic area of reconstruction were included in the data (discussed below). As a first step, the lowest attenuation value was set to zero for both sets. A histogram showing number of voxels per intensity value was generated for sample A (Fig. 1A). Since voxels have been shifted and will be filtered from this step forward, voxel values no longer represent original attenuation values. Therefore, arbitrary units of intensity value (I.V.) are assigned. The first algorithm, Tomo_optimize was written to perform the following five operations:

(1) Assign a user-determined intensity cut-off value for air versus solid.
(2) Apply an edge enhancement, 3-voxel by 3-voxel, non-unity-weight matrix filter.
(3) Apply a linear contrast transform.

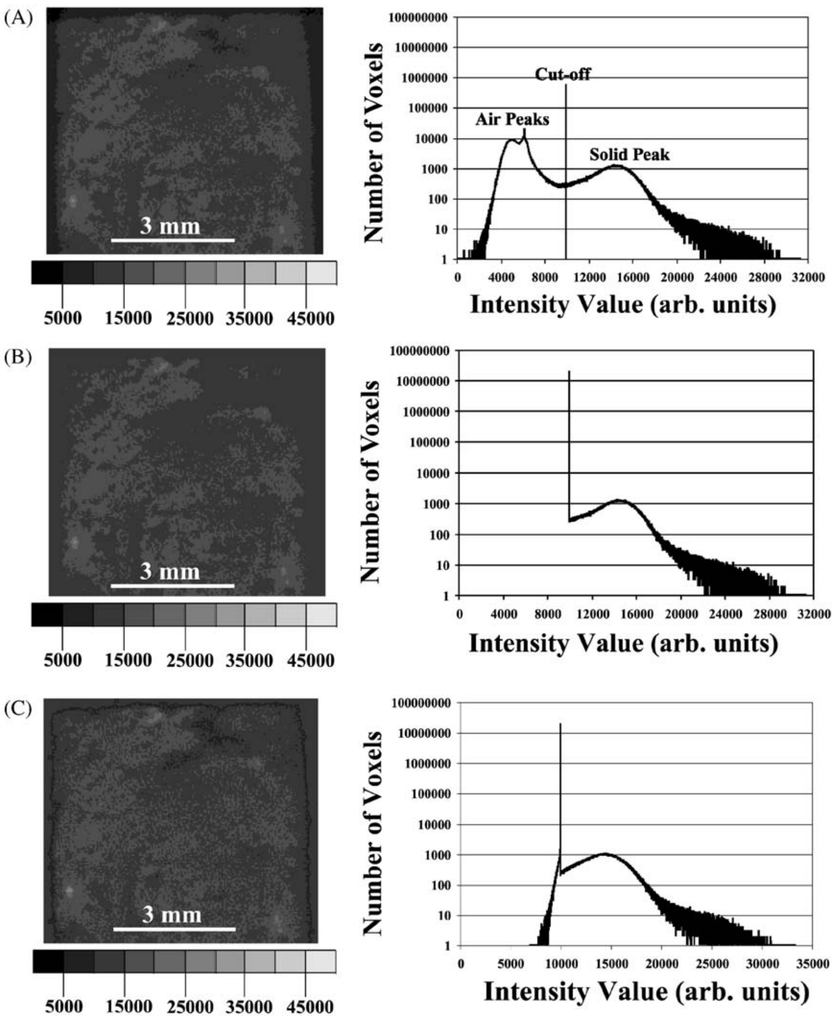

Fig. 1. Two-dimensional slices through a CμT volume and intensity value histograms after each step of Tomo_optimize. (A) Original volume histogram showing air peaks at 4500 I.V. and 6000 I.V. and a solid peak at 15,000 I.V., (B) original data after threshold determination of 10,000 I.V. and data shift to 10,000 I.V., (C) application of edge enhancement filter, (D) linear contrast transform using a 1.5 slope, (E) application of low-pass filter, and (F) voxels separated into solid or void space using a threshold of 17,400 I.V.

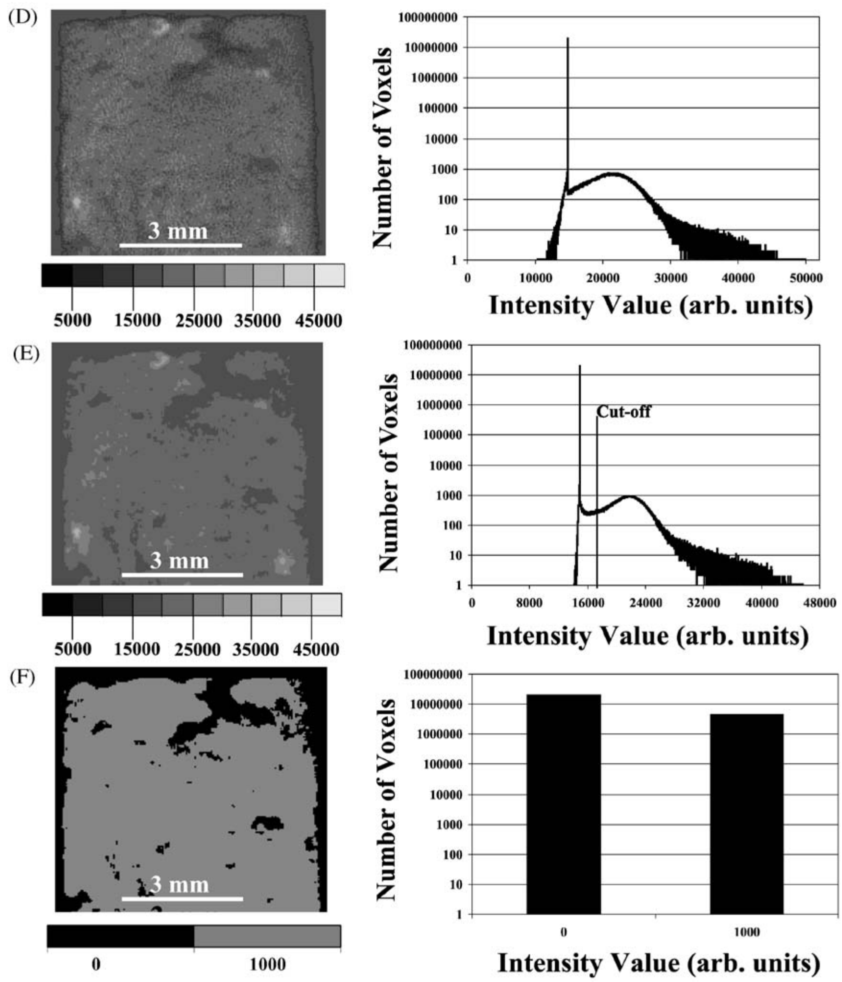

Fig. 1 (*continued*).

(4) Apply a low-pass, 3-voxel by 3-voxel, unity-weight matrix filter.
(5) Assign a user-determined intensity cut-off value for void space versus solid.

Each of these steps is explained briefly below.

(1) The two samples in this study consist predominately of sulfide minerals, which have high linear attenuation coefficient values. Void space and minerals have very different intensity values as indicated by the distinct peaks in Fig. 1A. There are two "air peaks" present in Fig. 1A. The peak at 6000 I.V. is air that surrounds the sample while the peak at 4500 I.V. represents voxels outside the area of tomographic reconstruction. Since voxels present in the peak at 4500 I.V. are lower in value than the voxels in the air peak (6000 I.V.), they will be below the intensity cut-off value between air and solid and therefore have no effect on volume analysis. An intensity cut-off value is chosen by maximum likelihood to separate air from solid material. There are several methods of choosing a cut-off value (also called thresholding) such as global or local thresholding (Oh and Lindquist, 1999). The program is written such that the user determines the method of thresholding and inputs the chosen cut-off value into the algorithm. All voxels equal to or less than the intensity cut-off value are set to that value (Fig. 1B).

(2) The second step of the algorithm is application of a two-dimensional edge enhancement, 3-voxel by 3-voxel, non-unity weight matrix filter. The edge enhancement procedure magnifies intensity value gradients between neighboring voxels within each z slice of the volume. Filtering is done in two dimensions rather than three dimensions because the matrix filter uses non-unity weighting to enhance contrast between solid and void space voxels. There is less averaging of voxels in two dimensions (9 voxels) compared to three dimensions (27 voxels) for which a greater range of grayscale voxels

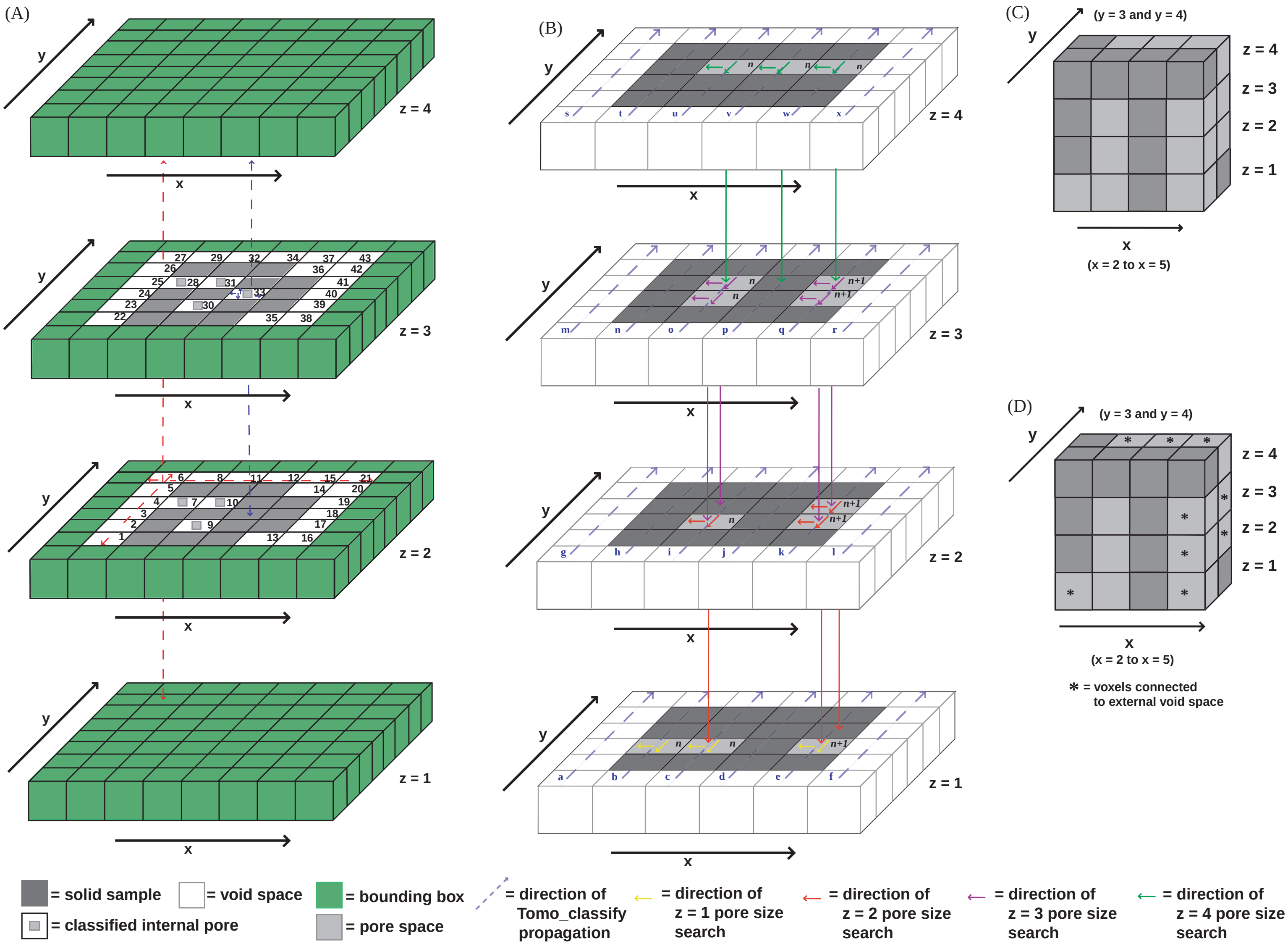

(A)
(B)
(C)
(D)
(y = 3 and y = 4)
(x = 2 to x = 5)
z = 4
z = 3
z = 2
z = 1
x
y
∗ = voxels connected to external void space
= solid sample
= void space
= bounding box
= classified internal pore
= pore space
= direction of Tomo_classify propagation
= direction of z = 1 pore size search
= direction of z = 2 pore size search
= direction of z = 3 pore size search
= direction of z = 4 pore size search

is averaged. Accentuation of gradients between solid and void space makes the image appear more pixilated, as seen by comparison of Figs. 1B and C.

(3) In the third step of the algorithm, a linear contrast stretch increases the range of intensity values in the entire volume by stretching the original intensity range over a larger range. The linear stretch was performed with a slope of 1.5 and intercept equal to 0, although any slope value can be entered into the program. Contrast increases with larger slope values. The edge-enhanced intensity values are set to the linearly stretched values. Comparison of the histograms in Figs. 1C and D shows an increase in the number of intensity values from the edge-enhanced range (26,863 I.V.) to the stretched range (40,294 I.V.), which increases contrast by spreading the voxels over a range that is 150% larger.

(4) The fourth step of the algorithm smooths the image by application of a two-dimensional low-pass, 3-voxel by 3-voxel, unity-weight matrix filter which computes the average value of a voxel based on its surrounding voxels for each z slice in the volume. The image in Fig. 1E appears less pixilated; however, edges between solid material and void space remain pronounced. The histogram of intensity values after smoothing shows a better-defined peak for solid voxels (Fig. 1E).

(5) Finally, a cut-off value determined by the user from the histogram in Fig. 1E is input into the program to assign a void space-solid cut-off value. We have chosen to use a binary classification where each voxel in the digital data set is assigned to one of two categories, either void space which includes voxels less than and equal to the cut-off value, or solid which includes voxels greater than the cut-off value (Fig. 1F). The sensitivity of this approach is discussed in Section 3.4.

3.2. Voxel classification

Within the optimized volumes, we have chosen three possible voxel classifications: external void space, solid material, and internal pore space, which allows us to determine connected and internal pores for a sub-volume of any size. Difficulty arises at a sample edge because in some cases the boundary contains pore space that should be included in the porosity calculation regardless of whether the edge is a physical boundary or a virtual edge. For this study, both samples were sectioned with a diamond saw, and therefore the edges were artificially straight. The edges of the volume selected for analysis, however, can be either physical edges (rough or smooth), or virtual edges. In order to classify a voxel as solid, internal pore space, or external void space, the program Tomo_classify first forms a bounding box completely encompassing the volume (data set input file) selected by the user for analysis (Fig. 2A). The input file may be the entire tomographic file or a smaller sub-volume file. Only voxels determined to be void space from the optimization program are considered. Void space is examined one voxel, one y column, and one z-slice at a time (voxels numbered 1–43 in order of consideration in Fig. 2A). Each edge voxel potentially has 6 linear connections in three dimensions ($\pm x$, $\pm y$, and $\pm z$) to the bounding box that can only be interrupted by voxels classified as solid. Voxels with 0, 1, 2, or 3 uninterrupted linear connections to the bounding box are classified as internal pore space based on the criterion that a voxel which is half or more surrounded by solid-classified voxels in three dimensions is part of the pore structure. Voxel 33 in Fig. 2A has one linear connection to the bounding box in the $+z$ direction, therefore it is classified as internal pore space. Voxel numbers 9 and 30 are classified as internal pore space and have two linear connections to the bounding box (Fig. 2A). An example of an internal pore space with three linear connections to the bounding box is shown in voxel numbers 28 and 31 (Fig. 2A).

Voxels with 4, 5, or 6 uninterrupted linear connections to the bounding box are classified as external void space. An example of a voxel with four linear connections to the bounding box is shown in voxel numbers 35 and 36 (Fig. 2A). Voxel number 37 in Fig. 2A has five linear connections to the bounding box and voxel 6 in Fig. 2A has six linear connections to the bounding box ($\pm x$, $\pm y$, and $\pm z$). All of the aforementioned voxels are classified as external void space. Total porosity is calculated based on this criterion of three or less connections classified as

Fig. 2. (A) Solid, external void space, and internal pore space are determined using Tomo_classify which first forms a bounding box around the volume (shown for a two z-slice volume). Only voxels that are void space are considered. Void space is examined one voxel, one y column, and one z slice at a time (voxels numbered 1–43 in order of consideration). Each voxel has a potential of 6 linear connections with the bounding box ($\pm x$, $\pm y$, $\pm z$). Linear connections to bounding box are only interrupted by solid sample voxels. Voxels with 0, 1 (voxel 33), 2, or 3 linear connections to bounding box are pore space and voxels with 4, 5, or 6 (voxel 6) linear connections to bounding box are outside air voxels. (B) Individual pores within the sample are determined by Tomo_analysis. Only voxels determined to be pore space by Tomo_classify are considered. Analysis for a four z-slice volume is shown. Algorithm begins in the bottom left corner of $z = 1$ and progresses by y columns (a–f). At each pore space voxel (x, y) voxels in $(x-1)$ and $(y-1)$ position are examined. If those voxels are pore space then (x, y) voxel is assigned the same number (n). If not, then voxel is assigned a new number ($n+1$ at $z = 1$). When algorithm progresses to $z = 2$, $(x-1)$, $(y-1)$, and $(z-1)$ in (x, y) position are considered. At $z = 4$ pore 1 is connected to pore 2. (C) Pore is relabeled as 1 and entire pore is shown to be 13 voxels in size. (D) Pore voxels connected to external void space are labeled as connected (*) and pore voxels that are not connected to external void space are interior pores.

internal void space. However, the criterion can be easily modified in the Fortran program. Output includes total porosity and the number of voxels in the entire volume that are classified as external void space, solid, and internal pore space. Note that if the user chooses a sub-volume in which all sides are not surrounded by outside air, the only voxel classifications in the output will be internal pore space and solid because the next algorithm depends on the classification of external void space to calculate pore connectivity.

3.3. Porosity and pore connectivity

The program Tomo_analysis determines the number of individual pores, individual pore volumes, total porosity (number of internal pore voxels divided by the number of solid voxels plus internal pore voxels), and pore connectivity. The first step determines the number of voxels within a pore. Only voxel connections between any of the 6 faces of a voxel are considered. For any voxel there are 6 faces, 12 edges, and 8 corners. The spatial resolution of these two data sets (57 μm) is not high enough to assume that a connection between voxel corners or edges is a valid one, although this criterion could be modified for higher resolution data sets. Shared corners have only one point of contact and shared edges have only one 21.6 μm long length of contact, whereas shared faces have a 466.6 μm^2 area of contact. All pore space was assigned a value of 0 in Tomo_classify. The volume is searched upwards (from $z = 1$ to 4) in the y direction (Fig. 2B) until the first 0 value voxel is found and assigned a value of n, where $n = 1$ initially. When the algorithm reaches the next 0-value voxel (x, y, z), it examines the $(x-1, y, z)$, $(x, y-1, z)$, and $(x, y, z-1)$ voxels. If any of these are 0-value voxels, the (x, y, z) voxel is assigned the same label n. If all of them are not 0-value voxels then a value of $n+1$ is assigned because there is no connection with a previously analyzed pore voxel. This procedure continues until all pore space voxels are assigned a label n greater than 0. Next, Tomo_analysis proceeds to pass through the sample volume again. At each (x, y, z) pore voxel the algorithm looks at the $(x \pm 1, y, z)$, $(x, y \pm 1, z)$, and $(x, y, z \pm 1)$ voxels. If any of those voxels are pore space and have a label n less than the (x, y, z) voxel, the (x, y, z) voxel is relabeled with the smaller n label. At the end of each pass through the sample, the algorithm again looks at the $(x \pm 1, y, z)$, $(x, y \pm 1, z)$, and $(x, y, z \pm 1)$ voxels and compares it to the (x, y, z) voxel. If the face-connected pore spaces all contain the same n label, the algorithm proceeds, or else it will begin to make passes through the sample again, until all face-connected pores are labeled the same (Fig. 2C). After having labeled the pore space voxels, the algorithm determines which pores are connected to the volume exterior. A pore is considered connected if any voxel within the pore has a shared face with a voxel of external void space. An interior pore is defined as a pore enclosed in all 6 directions by solid voxels. Thus the algorithm has successfully identified the pore in Fig. 2B as a single connected pore (Fig. 2D).

The second part of Tomo_analysis does the following:

(1) Tabulates the total number of interior pores and connected pores.
(2) Calculates the total porosity of interior pores and the total porosity of connected pores.
(3) Output consists of three files: one file for unconnected pores, one file for connected pores, and one file for the whole data set. The unconnected and connected files give the label assigned to each unconnected/connected voxel in one column. The label file gives the label assigned to each voxel in the data set (either unconnected pore, connected pore, solid, or external void space).

Porosity results from Tomo_analysis performed on samples A and B are shown in Table 1. Sample A has a porosity of $14.1 \pm 3.2\%$ and sample B has a porosity of $15.4 \pm 2.8\%$. For both samples A and B, the majority of total porosity ($>90\%$) is from one large connected pore. A sub-volume from each CμT sample volume was extracted and interior pores were plotted (Fig. 3). The physical pore space in sample A (Fig. 3A) has irregular shapes and sizes throughout the sub-volume. Sample B has one large irregular channel (Fig. 3B) with several smaller pores surrounding the channel. The large opening of the channel is shown on the right side of Fig. 3B. The channel branches in several directions in the middle of the volume and again at the left side of the volume. Even though both samples have similar total porosity, visualization in three dimensions points out differences in their physical structures.

Due to the high density of sulfide and sulfate minerals composing hydrothermal vent chimneys, data were collected at 40 keV incident X-ray energy, compared with 17–18 keV typically used for sandstones (Coker et al., 1996; Lindquist et al., 2000). Spatial resolution decreases as the energy increases much above 30 keV due to scattering and penetration in the scintillator screen. Therefore, achieving high spatial resolutions is more difficult with denser samples and small samples are preferable.

3.4. Algorithm sensitivity and computational efficiency

In the image optimization performed by the first algorithm, Tomo_optimize, input includes two intensity cut-off values determined by the user. These two values are entered into the program as the first cut-off value between air and solid (Fig. 1A), and a second value as a cut-off between void space and solid sample in the last step (Fig. 1F). Since the values are user-selected based

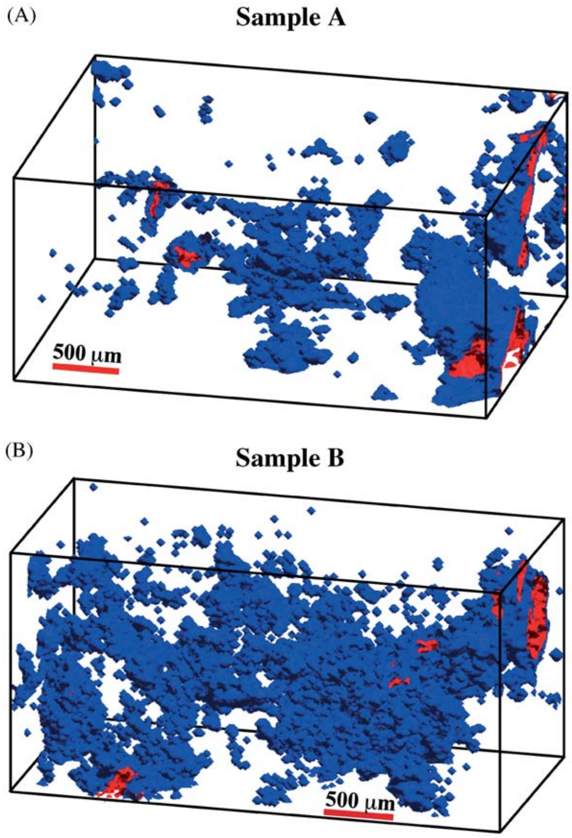

Fig. 3. Physical images of sub-volume from (A) sample A and (B) sample B in three dimensions showing pore space. Outer surfaces of pores are blue and pore interiors are red.

on intensity value histograms, they contribute to sensitivity and accuracy of the porosity and pore connectivity calculation. For this study, our method of choosing cut-off values was to use the intensity value histograms and maximum likelihood to determine cut-off values between peaks. First, a histogram of the original volume was created. The first cut-off value was determined and entered into Tomo_optimize while entering an arbitrary second cut-off value (a value must be entered for the program to run). At the completion of Tomo_optimize, an intensity value histogram was created from the low-pass filtered data set and the second cut-off value was determined by maximum likelihood. Tomo_optimize was run again using both user-determined cut-off values to get a final optimized volume.

In order to test algorithm sensitivity to the user-determined cut-off values, a range of intensity cut-off values was used in Tomo_optimize. As the first cut-off intensity value for the original data is increased above the air peaks (Fig. 4A), the amount of porosity also increases because some of the previously defined solid voxels are now included as air voxels (Fig. 4B). An increase in porosity from 9% to 44% occurs when the cut-off value is increased from 8000 I.V. to 12,000 I.V. The most dramatic increase in porosity occurs with cut-off values greater than 11,000 I.V. because those values are clearly part of the original data solid peak in Fig. 4A. Sensitivity to the initial cut-off value is especially severe for heterogeneous samples that have a wide range of mineral attenuation and therefore intensity values. In such cases, the difference in intensity values between air and solid will be small and peak overlap will increase, making it more difficult to determine a cut-off value.

In order to test the capability of the algorithm to resolve the smallest pores, pore volume from individual pores was compared to percentage of total porosity for both samples (Fig. 5). Each sample contains one large connected pore that contributes over 90% to the total porosity. Plots in Fig. 5 were enlarged to focus on pores that were from 1 to 280 voxels in size. Pore volumes composed of three voxels or less in both samples (pore volumes of 10,078–30,233 μm^3) contribute a slightly larger amount to overall porosity (0.5–0.9%) than the contribution to overall porosity of larger pores (pores from 4 to 280 voxels in size), which each contribute less than 0.1% to the total porosity. Porosity from pores that are one, two, and three voxels in size was consistently 0.5–0.9% of the total porosity over the range of cut-off intensity values. The consistency in contribution from this pore volume range to total porosity, independent of the cut-off value, shows that the algorithms are capable of resolving pores that are equal to one voxel in size and that these small pores are not simply "noise". Resolution of small pores is accomplished by removing noise and artifacts (irregularities) and by the binary classification done in Tomo_optimize. However, since two-dimensional spatial resolution was 57 μm for this study, porosity from pores <4 voxels (<1% of total porosity) was omitted from the results. This sensitivity test indicates that the algorithms are capable of resolving pores that are greater than and equal to one voxel in size, and that the porosity calculation is most sensitive to the cut-off value chosen for air versus solid in the first step.

The second cut-off value applied after the low-pass filter (Fig. 1E) is a cut-off between solid sample and void space. To test algorithm sensitivity to the second cut-off value, movement of each voxel was tracked throughout the filtering process (before determining the second cut-off value). Low-pass filtered voxels that were originally part of the air peaks are shown in red and low-pass filtered voxels that were originally part of the solid peak are shown in yellow (Fig. 4C). From 17,200 I.V. to 19,000 I.V., voxels originally included in air intersect the x-axis. Increasing the cut-off intensity value through this range, which is much smaller than the range for the first intensity cut-off, resulted in an increased porosity of

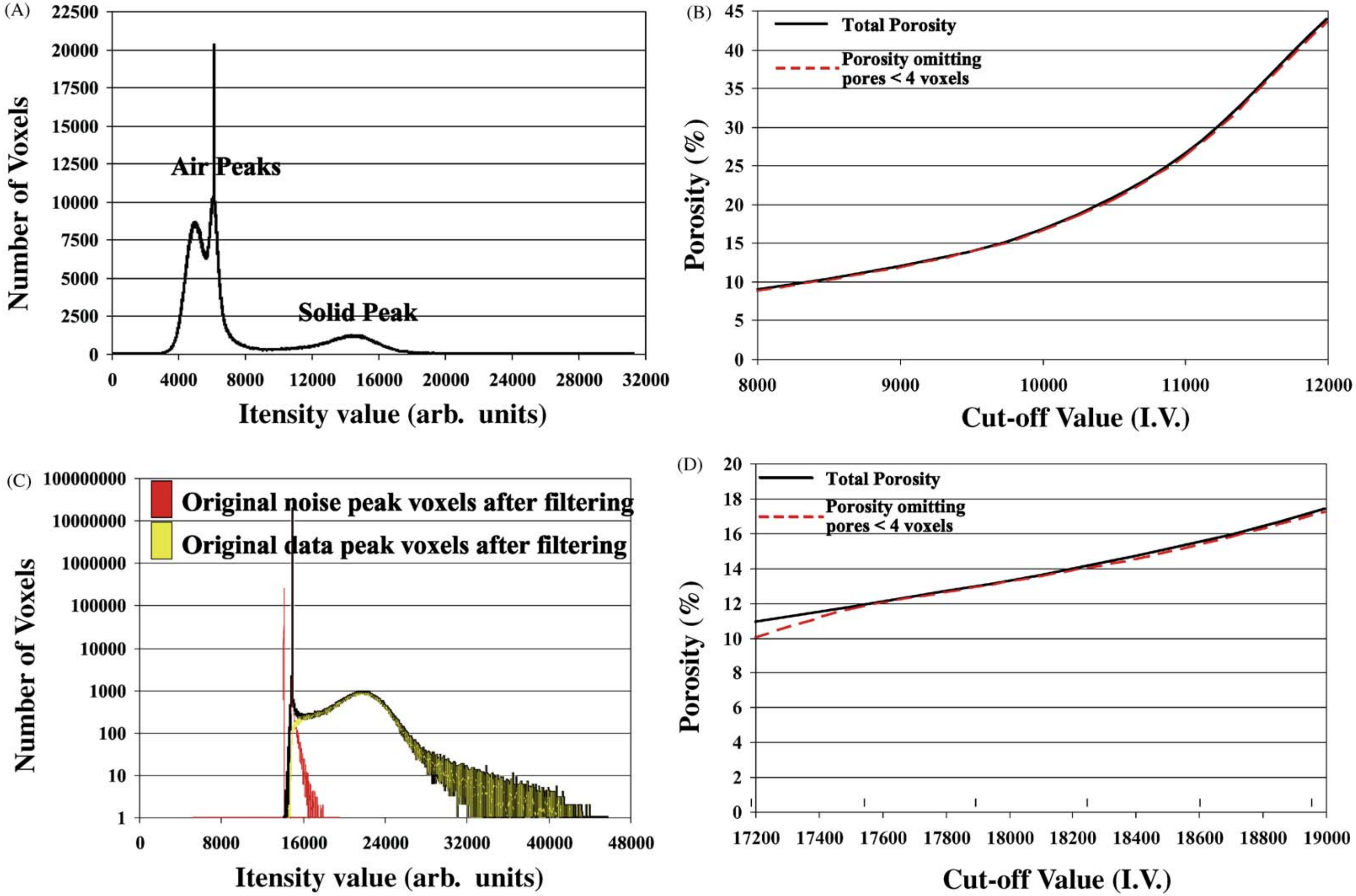

Fig. 4. Algorithm sensitivity as a function of user input threshold intensity values. (A) Original data set histogram shows range from 8000 I.V. to 12,000 I.V. of possible peak overlap between air peak at 6000 I.V. and solid peak at 15,000 I.V. (B) Porosity calculated with air versus solid cut-off values in range of 8000 I.V. to 12,000 I.V. increases with increasing intensity value cut-off. Porosity from pores less than 4 voxels contributes from 0.5% to 0.9% of total porosity over the range of cut-off values. (C) Histogram calculated after low-pass filter (black) is partitioned into two separate histograms of low-pass filtered voxels that were initially found in air peaks of the original volume (red) and low-pass filtered voxels that were part of the original volume solid peak (yellow). A range of 17,200 I.V. to 19,000 I.V. in peak overlap (where red histogram intersects *x*-axis) is tested for the cut-off value. (D) Porosity increases by 6.5% when calculated over range of cut-off values. Porosity from pore volumes less than 4 voxels contributes from 0.7% to 0.85% of total porosity over cut-off range.

6.5% because voxels initially classified as solid are now classified as void space (Fig. 4D). When pores that are three voxels and less were omitted, porosity increased with cut-off value by 7.5%. Both user-determined intensity cut-off values contribute to algorithm sensitivity, but the algorithms are more sensitive to the first cut-off value (air or solid) rather than the second cut-off (void space or solid) because contrast has been enhanced by Tomo_optimize between application of the first and second cut-off values. Both cut-off intensity values are

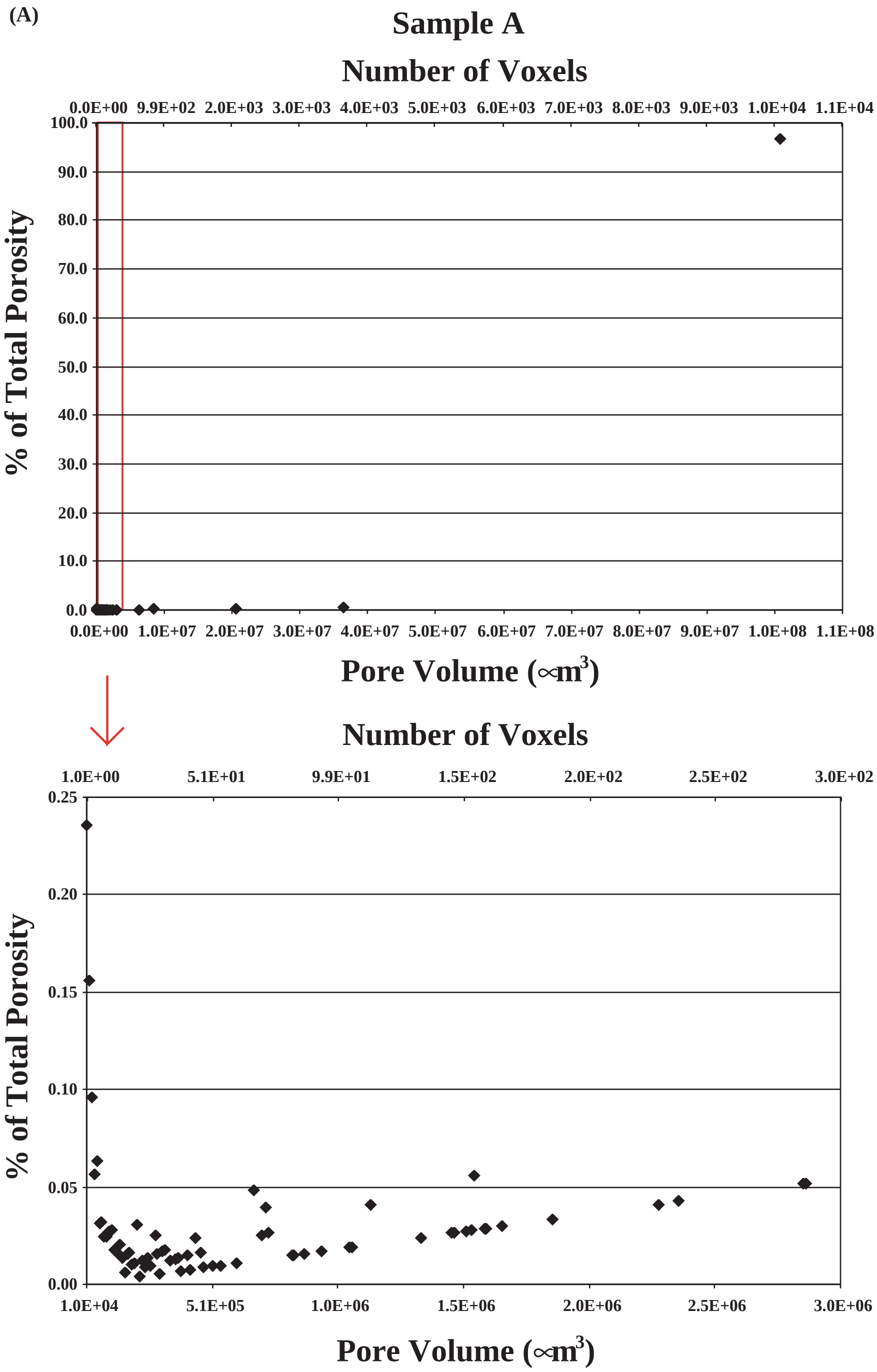

Fig. 5. Pore volume versus percent of total porosity from each pore volume for (A) sample A and (B) Sample B. In this study, 1 voxel = 10,078 μm^3 and is the smallest resolvable volume.

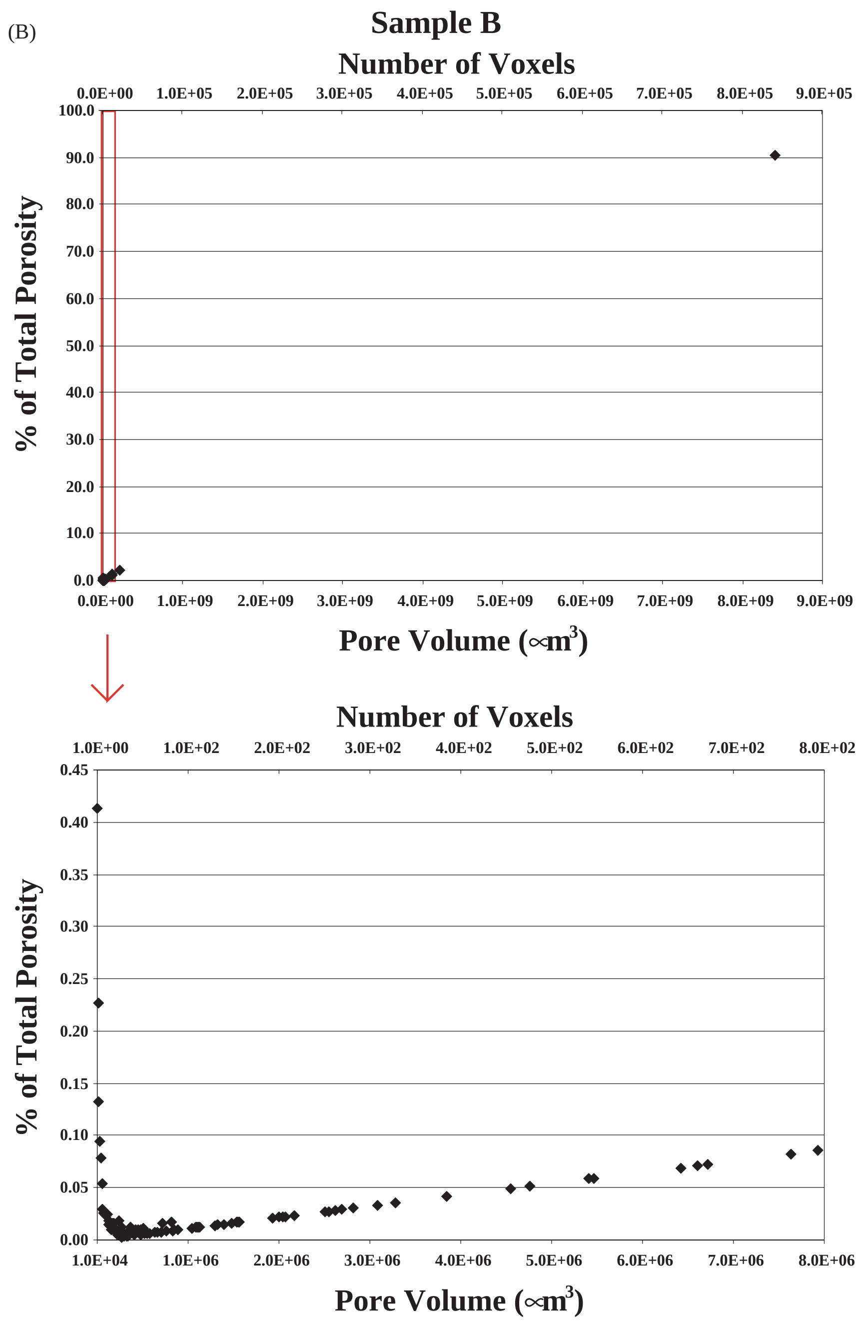

Fig. 5 (*continued*).

used to calculate the error reported with the algorithm porosity results. For this study, we used two extreme choices of cut-off values (from the range of peak overlap). The difference in porosity between the two cut-off values was calculated and reported as the error.

For a volume that is $414 \times 414 \times 147$ voxels, computational time for Tomo_optimize is 5 min, Tomo_classify is 8 min, and Tomo_analysis is 21 min using a SUN Ultra 10 workstation with an UltraSPARC-II™ processor. Output files from Tomo_optimize include a filtered data set that can be processed to create two-dimensional images of each slice and histogram data for each step of the filtering process as shown in Fig. 1. Tomo_classify output files include a value for total porosity and a voxel-classified data set that can be manipulated to create two-dimensional images of each slice. Tomo_analysis output files include the final analyzed data set in addition to total porosity of connected pores, total porosity of interior pores, and the number of voxels that are solid, internal pore space, and external void space.

4. Conclusions

The algorithms described here are useful, flexible tools for examining three-dimensional pore structure, porosity, and pore connectivity in structurally and chemically complex samples using synchrotron CμT. Owing to the variability in data sets collected at different energies on different beamlines, image optimization is important to remove artifacts and increase volume uniformity before the analysis of porosity and pore connectivity. Our package of algorithms accomplishes image optimization based on user input, voxel classification at the voxel level, and analysis of porosity and pore connectivity on a generic data volume. They have the flexibility to analyze total physical volumes or virtual sub-volumes, and allow the user to visualize the three-dimensional results. The algorithms are written in Fortran 90, which is an inexpensive program that is available on all operating systems and friendly to user editing. These algorithms are computationally fast: ~ 34 min for a $414 \times 414 \times 147$ voxel volume on a Sun Ultra 10 Workstation with an UltraSPARC-II™ processor.

In this study, we used a binary classification of solid or void space based on cut-off values chosen by the user before and after image processing to enhance contrast and edge features. Sensitivity tests showed that the porosity calculation is more dependent on the first cut-off intensity value for air and solid assigned before image processing than on the second cut-off. As such, users may choose to perform their own sensitivity tests for cut-off values, particularly if intensity values are clustered. The approach of contrast enhancement and binary classification, rather than mixed voxel classification, is appropriate for the high resolution achievable with synchrotron CμT. We showed that the algorithms are capable of resolving pores one voxel in size for the resolution of this study ($\sim 57\,\mu m$). Because resolution is limited by sample size in CμT (i.e., a larger sample volume results in larger voxel size), it is important to consider the trade-off between the optimum sample volume and the desired resolution for a particular study. For natural mineral samples, attenuation values vary considerably because of differences in mineral composition and density. Our set of algorithms allows users to process data sets with a wide range of grayscales, including subtraction of volumes collected at different energies, in order to enhance contrast between minerals in addition to contrast between solid and pore space. Synchrotron CμT is finding many applications in the geosciences and its capabilities will continue to increase with improvements in data collection and analysis methods.

Acknowledgements

The authors wish to thank Deborah S. Kelley from the University of Washington for the samples used for analysis. We acknowledge Scot Thompson and Mike Jew from Arizona State University for help with CμT data collection and preprocessing, and to the reviewers for constructive comments. This research was supported by NASA NCC2-1051 and NSF EAR-0073984. Use of the Advanced Photon Source was supported by the US Department of Energy, Office of Science, Office of Basic Energy Sciences, under Contract No. W-31-109-Eng-38.

References

Ackerman, J.L., Ellingson, W.A., 1991. Advanced Tomographic Imaging Methods for the Analysis of Materials. Materials Research Society, Pittsburgh, 218pp.

Ashbridge, D.A., 2002. Chemical and physical analysis of seafloor hydrothermal vent chimneys. M.Sc. Thesis, Arizona State University, Tempe, Arizona, 67pp.

Ballester, M.A.G., Zisserman, A.P., Brady, M., 2002. Estimation of the partial volume effect in MRI. Medical Image Analysis 6 (4), 389–405.

Baruchel, J., Lodini, A., Romanzetti, S., Rustichelli, F., Scrivani, A., 2001. Phase-contrast imaging of thin biomaterials. Biomaterials 22 (12), 1515–1520.

Bonse, U., Busch, F., 1999. X-ray computed microtomography (μCT) using synchrotron radiation (SR). Progress in Biophysics and Molecular Biology 65 (1/2), 133–169.

Choi, H.S., Haynor, D.R., Kim, Y., 1991. Partial volume tissue classification of multichannel magnetic resonance images-a mixel model. IEEE Transactions on Medical Imaging 10 (3), 395–407.

Coker, D.A., Torquato, S., Dunsmuir, J.H., 1996. Morphology and physical properties of Fontainebleau sandstone via a tomographic analysis. Journal of Geophysical Research—Solid Earth 101 (B8), 17497–17506.

Delaney, J.R., Kelley, D.S., Mathez, E.A., Yoerger, D.R., Baross, J., Schrenk, M.O., Tivey, M.K., Kaye, J., Robigou, V., 2001. "Edifice Rex" sulfide recovery project: analysis of submarine hydrothermal, microbial habitat. EOS Transactions AGU 82(6), 67, 72–73.

Delerue, J.P., Perrier, E., Yu, Z.Y., Velde, B., 1999. New algorithms in 3D image analysis and their application to the measurement of a spatialized pore size distribution in soils. Physics and Chemistry of the Earth Part A—Solid Earth and Geodesy 24 (7), 639–644.

Green, W.B., 1983. Digital Image Processing: A Systems Approach. Van Nostrand Reinhold Co., New York, 192pp.

Ketcham, R.A., Carlson, W.D., 2001. Acquisition, optimization and interpretation of X-ray computed tomographic imagery: applications to the geosciences. Computers & Geosciences 27 (4), 381–400.

Kinney, J.H., Nichols, M.C., Bonse, U., 1991. Nondestructive imaging of materials microstructures using X-ray tomographic microscopy. In: Ackerman, J.L., Ellingson, W.A. (Eds.), Advanced Tomographic Imaging Methods for the Analysis of Materials. Materials Research Society, Pittsburgh, pp. 81–95.

Lindquist, W.B., Lee, S.M., Coker, D.A., Jones, K.W., Spanne, P., 1996. Medial axis analysis of void structure in three-dimensional tomographic images of porous media. Journal of Geophysical Research—Solid Earth 101 (B4), 8297–8310.

Lindquist, W.B., Venkatarangan, A., 1999. Investigating 3D geometry of porous media from high resolution images. Physics and Chemistry of the Earth Part A—Solid Earth and Geodesy 24 (7), 593–599.

Lindquist, W.B., Venkatarangan, A., Dunsmuir, J., Wong, T.F., 2000. Pore and throat size distributions measured from synchrotron X- ray tomographic images of Fontainebleau sandstones. Journal of Geophysical Research—Solid Earth 105 (B9), 21509–21527.

Marshall, C., 1982. The Physical Basis of Computed Tomography. W.H. Green, St. Louis, 171pp.

Oh, W., Lindquist, W.B., 1999. Image thresholding by indicator kriging. IEEE Transactions on Pattern Analysis and Machine Intelligence 21 (7), 590–602.

Pratt, W.K., 1978. Digital Image Processing. Wiley, New York, 750pp.

Proussevitch, A.A., Sahagian, D.L., 2001. Recognition and separation of discrete objects within complex 3D voxelized structures. Computers & Geosciences 27 (4), 441–454.

Rivers, M.L., Sutton, S.R., Eng, P., 1999. Geoscience applications of X-ray computed microtomography. In: Bonse, U. (Ed.), Developments in X-ray Tomography 2. SPIE, Bellingham, pp. 78–86.

Roll, S.A., Colchester, A.C.F., Summers, P.E., Griffin, L.D., 1994. Intensity-based object extraction from 3D medical images including a correction for partial volume errors. In: Proceedings of the Fifth British Machine Vision Conference, Guildford, UK, pp. 205–214.

Santago, P., Gage, H.D., 1993. Quantification of MR brain images by mixture density and partial volume modeling. IEEE Transactions on Medical Imaging 12 (3), 566–574.

Soltanian-Zadeh, H., Windham, J.P., Yagle, A.E., 1993. Optimal transformation for correcting partial volume averaging effects in magnetic resonance imaging. IEEE Transactions on Nuclear Science 40 (4), 1204–1212.

Spanne, P., Thovert, J.F., Jacquin, C.J., Lindquist, W.B., Jones, K.W., Adler, P.M., 1994. Synchrotron computed microtomography of porous media: topology and transports. Physical Review Letters 73 (14), 2001–2004.

Wellington, S.L., Vinegar, H.J., 1987. X-ray computerized tomography. Journal of Petroleum Technology 39 (8), 885–898.